

Construction of Magnetic Nanochains to Achieve Magnetic Energy Coupling in Scaffold

Cijun Shuai

JiangXi University of Science and Technology

Xuan Chen

JiangXi University of Science and Technology

Chongxian He

Central South University

Guowen Qian

JiangXi University of Science and Technology

Yang Shuai

Huazhong University of Science and Technology

Jia Yao

Central South University

Wendi Xu

Central South University

Shuping Peng

Central South University

Youwen Deng

Central South University

Wenjing Yang (✉ yangwenjing@jxust.edu.cn)

JiangXi University of Science and Technology <https://orcid.org/0000-0002-4945-8659>

Research Article

Keywords: Magnetic microenvironment, Fe₃O₄ nanoparticles, Magnetic nanochains, Magnetic energy coupling, Bone scaffold

Posted Date: March 22nd, 2022

DOI: <https://doi.org/10.21203/rs.3.rs-1448231/v1>

License:   This work is licensed under a Creative Commons Attribution 4.0 International License.

[Read Full License](#)

Abstract

Background: Fe_3O_4 nanoparticles are highly desired for constructing endogenous magnetic microenvironment in scaffold to accelerate bone regeneration due to their superior magnetism. However, their random arrangement easily leads to mutual consumption of magnetic poles, thereby weakening the magnetic stimulation effect.

Methods: In this study, magnetic nanochains are synthesized by magnetic-field-guided interface co-assembly of Fe_3O_4 nanoparticles. In detail, multiple Fe_3O_4 nanoparticles are aligned along the direction of magnetic force lines and are connected in series to form nanochain structures under an external magnetic field. Subsequently, the nanochain structures are covered and fixed by depositing a thin layer of silica (SiO_2), and consequently forming linear magnetic nanochains ($\text{Fe}_3\text{O}_4@ \text{SiO}_2$). The $\text{Fe}_3\text{O}_4@ \text{SiO}_2$ nanochains are then incorporated into poly L-lactic acid (PLLA) scaffold prepared by selective laser sintering technology.

Results: The results show that the $\text{Fe}_3\text{O}_4@ \text{SiO}_2$ nanochains with unique core-shell structure are successfully constructed. Meanwhile, the orderly assembly of nanoparticles in the $\text{Fe}_3\text{O}_4@ \text{SiO}_2$ nanochains enable to form magnetic energy coupling and obtain a highly magnetic micro-field. The *in vitro* tests indicate that the PLLA/ $\text{Fe}_3\text{O}_4@ \text{SiO}_2$ scaffolds exhibit superior capacity in enhancing cell activity, improving osteogenesis-related gene expressions, and inducing cell mineralization compared with PLLA and PLLA/ Fe_3O_4 scaffolds.

Conclusion: In short, the $\text{Fe}_3\text{O}_4@ \text{SiO}_2$ nanochains endow scaffolds with good magnetism and cytocompatibility, which have great potential in accelerating bone repair.

Introduction

Recent scaffolds lack the capacity to effectively modulate cell growth or tissue reconstruction, resulting in slow bone regeneration and even failure of bone implantation [1–3]. It is well known that cells are magnetically sensitive due to the diamagnetism of cell membranes [4], and exposure to magnetic fields served to alter membrane flux and regulate ion channels and biochemical pathways [5, 6]. In this case, a series of cell behaviors will be mediated. Inspired by this, it is significant to construct an endogenous magnetic microenvironment in bone scaffold to mediate cell behaviors and tissue regeneration via magnetic stimulation.

As a typical magnetic material, Fe_3O_4 nanoparticles have been widely used in tissue engineering field due to their superior magnetic properties and good biocompatibility [7]. In addition, Fe_3O_4 nanoparticles enable to decompose into oxygen and iron in the body and can be easily removed from the body after degradation by oxygen transport and metabolism [8, 9]. The introduction of Fe_3O_4 nanoparticles into bone scaffolds is expected to construct an endogenous magnetic microenvironment to enhance cell activity and accelerate cell growth. It is worth noting that the random arrangement of Fe_3O_4 nanoparticles

in scaffold easily leads to mutual repulsive of magnetic poles between adjacent nanoparticles, thereby weakening the magnetic strength. In this case, the scaffold cannot fully exert its regulation on cell behaviors.

The directional assembly of Fe_3O_4 nanoparticles into ordered nanochain structures is expected to solve the above problem. Under external magnetic field, the internal magnetic dipole moment of Fe_3O_4 nanoparticles enable to be rapidly deflected to the direction of magnetic field [10, 11]. Moreover, the attractive magnetic dipole interaction drives multiple Fe_3O_4 nanoparticles to assemble into ordered magnetic nanochain structures along with magnetic force lines [12, 13]. Compared with randomly arranged Fe_3O_4 nanoparticles, the magnetic nanochain structure can realize the magnetic energy coupling between the nanoparticles, thereby enhancing the magnetic strength [14–16]. Li et al. synthesized uniform linear cobalt nanochains with a coating layer of polyvinylpyrrolidone in aqueous solution under an external magnetic field [17]. Zhang et al. synthesized one-dimensional nickel nanochains by dropping method [18].

In this study, $\text{Fe}_3\text{O}_4@SiO_2$ magnetic nanochains were synthesized utilizing a magnetic-field-guided interface co-assembly of nanoparticles. In short, Fe_3O_4 nanoparticles were firstly coated with a layer of protective SiO_2 film. Then, the above products were aligned and assembled into nanochains under an external magnetic field. Thereafter, the nanochains were fixated by further depositing with a layer of SiO_2 to permanent keep their structure. The microscopic morphology, chemical composition, and physicochemical properties of $\text{Fe}_3\text{O}_4@SiO_2$ were analyzed. Then, the $\text{Fe}_3\text{O}_4@SiO_2$ were loaded into PLLA scaffold which prepared using selective laser sintering (SLS). The cell activity, osteogenic differentiation and mineralization abilities induced by the scaffolds were investigated and analyzed in detail. Moreover, the osteogenesis-related gene expressions of runt-related transcription factor-2 (Runx2), osteopontin (OPN), osteocalcin (OCN) and osterix (OSX) of cells were assessed. Additionally, the stimulation mechanism of the magnetic scaffold on cells was also discussed in depth.

Experimental Sections

Materials

Medical-grade PLLA powders were obtained from Shenzhen Polymtek Biomaterial Co., Ltd. (Shenzhen, China). Fe_3O_4 nanoparticles with an average diameter of 100 nm, tetraorthosilicate (TEOS), sodium citrate dihydrate ($\text{C}_6\text{H}_5\text{Na}_3\text{O}_7 \cdot 2\text{H}_2\text{O}$), sodium hydroxide (NaOH) and concentrated ammonia solution ($\text{NH}_3 \cdot \text{H}_2\text{O}$, 28 wt.%) were purchased from Aladdin Chemistry Co. Ltd. (Shanghai, China). The above chemicals were applied as received without further purification.

Synthesis of one-dimensional $\text{Fe}_3\text{O}_4@SiO_2$ nanochains

The $\text{Fe}_3\text{O}_4@SiO_2$ nanochains were prepared through the magnetic-field-guided interface co-assembly of Fe_3O_4 nanoparticles, as shown in Fig. 1. The synthesis procedure was partly based on A. Saha et al [19–

21]. First, 20 mg of Fe₃O₄ nanoparticles was dispersed in 60 mL ethanol-aqueous solution by ultrasonication for 20 min. Subsequently, 5 mL of ammonia solution (28 wt.%) was dropped into the resulting solution with mechanical agitating (800 rpm) for 30 min. Then, the agitating speed was reduced to 300 rpm, and 10 mL of ethanol solution with TEOS ($V_{\text{ethanol}}:V_{\text{TEOS}}=9:1$) were dropped in the solution to coat Fe₃O₄ nanoparticles with a layer of protective SiO₂ film in the early stage of the sol-gel reaction of TEOS. After reaction for 15 min, the above solution was exposed in a static magnetic field (55 mT-65 mT) for 2 min to induce the linear arrangement of Fe₃O₄ nanoparticles without stirring, forming nanochain structures. After standing for another 10 min, the nanochain structures were further coated by SiO₂. Finally, the fixated core-shell Fe₃O₄@SiO₂ magnetic nanochains were obtained after magnetically collection, cleaning, and drying.

Preparation of scaffolds

For comparison, PLLA, PLLA/Fe₃O₄ and PLLA/Fe₃O₄@SiO₂ scaffolds were respectively fabricated. Prior to fabricating, PLLA/Fe₃O₄@SiO₂ and PLLA/Fe₃O₄ powders were prepared as follows. 4.6 g of PLLA powders and 0.4 g of Fe₃O₄@SiO₂ nanochains were added to a beaker containing 30 mL of ethanol and then ultrasound for 30 min, following by vigorously stirring 1 h to obtain dispersed suspensions. Subsequently, the suspensions were vacuum dried for 24 h at 65 °C, obtaining PLLA/Fe₃O₄@SiO₂ powders. Meanwhile, PLLA/Fe₃O₄ powders were also prepared in the same way.

The representative PLLA/Fe₃O₄@SiO₂ scaffold with honeycomb structure was fabricated via SLS technology. In detail, the PLLA/Fe₃O₄@SiO₂ powders were paved on the powder bed and selectively laser scanned according to the designed three-dimensional model, with laser power at 2.5 W, scanning speed at 100 mm/s and scanning distance at 0.24 mm [22, 23]. The modeling platform gradually descended with each layer of powders was sintered until the scaffold was completely formed.

Measurements and characterization

The morphologies of the Fe₃O₄@SiO₂ nanochains were observed by transmission electron microscope (TEM, TALOS F200X, USA). The chemical structure, compositions and crystal structures of the Fe₃O₄@SiO₂ or/and Fe₃O₄ powders were detected by X-ray photoelectron spectrometer (XPS, EscaLab 250Xi, USA), Fourier transform infra-red spectrometer (FTIR, FTIR 850, China) and X-ray diffractometer (XRD, D/MAX-RA, Japan). The magnetic properties of Fe₃O₄@SiO₂ and Fe₃O₄ powders were evaluated using a vibrating sample magnetometer (VSM, LakeShore7404, USA). Water contact angle on PLLA, PLLA/Fe₃O₄ and PLLA/Fe₃O₄@SiO₂ scaffolds were assessed using an optical contact angle meter (DM-501, Japan).

Cytocompatibility

The PLLA, PLLA/Fe₃O₄, PLLA/Fe₃O₄@SiO₂ scaffolds ($\varphi 8 \times 2 \text{ mm}^3$) were sterilized by immersing in 70% ethanol solution for 2 h and irradiating with UV for 12 h. Then, the sterilized scaffolds were individually

placed in 48-well culture plates. MG-63 cells (Sigma, Shanghai, China) were selected to investigate the cytocompatibility of scaffolds. MG-63 cells cultured in Dulbecco's Modified Eagle's Medium (DMEM) were washed with D-Hanks solution three times and were digested with trypsin. The resulting solution were centrifuged at 1000 r/min for 5 min. The cell suspension was diluted to 8×10^3 cells/mL. All the cells were incubated in a humidified condition with 5% CO₂ at 37°C.

The cells at a density of 4×10^3 cells/well were incubated on the surface of sterilized scaffolds in 48-well plates containing DMEM, in which the DMEM was updated daily. After incubating for 3 and 7 days, each cell-scaffold sample was washed with PBS three times, and then immersed in 5% glutaraldehyde for 30 min to fix cells. Thereafter, the cell-scaffold samples were dehydrated with 30%, 50%, 70%, 80%, 90%, 95% and absolute ethyl alcohol in sequence and dried for 12 h at room temperature. After coated with gold, the cell morphology on each scaffold was observed by scanning electron microscope (SEM).

Cell viabilities on the scaffolds were studied by a live/dead staining kit (Beyotime, China). At the specified time (3 and 7 days), the culture medium was removed, and the cells were detached from scaffolds and rinsed using PBS three times. Subsequently, the cells were stained with 2 μM Calcein-AM for 30 min at 37 °C. Finally, the stained cells were visualized using a fluorescence microscope (Olympus, Japan).

Cell proliferation was quantitatively assessed using Cell Counting Kit-8 (CCK-8, Beyotime, China) assay. The cell-scaffold samples were harvested from culture medium after 1, 4 and 7 days of cultivating. Then, the samples were washed with PBS and transferred into 96-well plates containing 100 μL CCK-8 reagent. After incubating for 2 h, the absorbance of the solution was detected utilizing a microplate reader (Thermal, USA) at 450 nm. Each group was carried out three parallel experiments.

The alkaline phosphatase (ALP) activity of the cells on scaffolds was determined to assess the osteogenic differentiation. After incubating for 7 days, the harvested cells from samples were washed with PBS 3 times and fixed with 4% paraformaldehyde for 15 min. Then, ALP staining kit (Beyotime, China) was dropped to stain the cells, and the stained cells were monitored using an inverted microscope (TE2000U, Japan).

The mineralization nodules of MG-63 cells cocultured with scaffolds were qualitatively investigated using Alizarin Red staining. The cells were seeded on scaffolds in 6-well plates for 7 days at a density of 1×10^4 cells/mL. After that, the cell-scaffold samples were fixed using 4% paraformaldehyde and rinsed with PBS. Subsequently, the samples were stained with 0.04 M Alizarin Red for 10 min. After rinsing, the samples were observed under a light microscope.

Scaffold-mediated cell differentiation and osteogenesis were further studied. For this, the expression of several relative genes containing runt-related transcription factor-2 (Runx2), osteopontin (OPN), osteocalcin (OCN) and osterix (OSX) were detected with quantitative real-time polymerase chain reactions (RT-PCR). After incubating for 3 and 7 days, the RNA isolation of cells was employed using TRIzol reagent, and then the RNA was reverse transcribed to cDNA using PrimeScript 1st strand cDNA synthesis

kit. Finally, the levels of Runx2, OPN, OCN and OSX were calculated using the $2^{-\Delta\Delta Ct}$ method. Each sample was analyzed three times.

Statistical analysis

All data were conducted by Student's *t*-test for independent samples and presented as means \pm standard deviation, where $**p < 0.01$ and $*p < 0.05$ represented significant difference.

Results

Fe₃O₄@SiO₂ nanochains

The representative one-dimensional structure of the Fe₃O₄@SiO₂ nanochains were observed using TEM. As shown in Figs. 2a and 2b, the Fe₃O₄@SiO₂ nanochains presented a unique core-shell structure, in which Fe₃O₄ nanoparticles served as cores with a diameter of about 100 nm and SiO₂ layers served as shells with a thickness of about 25 nm. Based on Fast Fourier transform (FFT, Figs. 2c and 2d), the interplanar distance between adjacent lattice fringes was 0.25 nm, which was in great agreement with the (311) lattice planes of Fe₃O₄. Moreover, the diffraction rings depicted in the selected area electron diffraction (SAED) patterns respectively corresponded to the (220), (311), (400), (440) and (422) lattice planes of cubic Fe₃O₄ (Fig. 2e). The Si, Fe and O elements were clearly exhibited in the elemental mapping images (Figs. 2f-i). Particularly, the distribution of Si and Fe elements further confirmed the shell-core structure of the nanochains. The results confirmed that the Fe₃O₄ nanoparticles could be induced to align in a nanochain though magnetic dipolar interaction under external magnetic field.

Magnetic field distribution around single Fe₃O₄ nanoparticle and nanochain in the same direction of external magnetic field was analyzed using finite element method (COMSOL Multiphysics), as shown in Figs. 3a-c. It could be seen that the magnetic dipole moment of a Fe₃O₄ nanoparticle reached a saturated value under the adequately strong magnetic field (Fig. 3a). When the centerline between two adjacent nanoparticles was aligned with the direction of the external magnetic field, the dipole-dipole interaction was attractive (Fig. 3b). When the interaction energy was large enough to overcome thermal fluctuations, the magnetic dipole-dipole force drove the self-assembly of nanoparticles into nanochains along the dipole moment (Fig. 3c). In this case, the dipole-dipole coupling reached the maximum. Therefore, the magnetism of nanochains can be regarded as the magnetic energy coupling between nanoparticles.

The magnetic properties of Fe₃O₄ nanoparticles and Fe₃O₄@SiO₂ nanochains were detected and presented in Fig. 3d. Magnetization curves confirmed the superparamagnetism of nanoparticles and nanochains due to the absence of hysteresis. The nanochains preserved their superparamagnetism during the synthetic processing from superparamagnetic nanoparticles, which was an important advantage for their applicability in biomedicine [24, 25]. The saturation magnetization of Fe₃O₄ was 52.2 emu/g. The relatively low saturation magnetization of Fe₃O₄@SiO₂ was due to the introduction of non-

magnetic SiO₂ shells decreased the weight ratio of Fe₃O₄ in Fe₃O₄@SiO₂ [26]. This phenomenon was also discovered by M. Tarhini and A. Bitar et al [20, 21].

XPS spectra of Fe₃O₄@SiO₂ nanochains were presented in Fig. 3e. The typical Fe2p, O1s and Si2p peaks were clearly observed (Fig. 3e₁). In detail, the peaks centered at 711.4, 723.0 and 726.0 eV were respectively corresponded to Fe²⁺2p_{3/2}, Fe²⁺2p_{1/2} and Fe³⁺2p_{1/2} of Fe₃O₄ (Fig. 3e₂), while the peaks centered at 102.7 and 104.2 eV were assigned to Si-OH and Si-O-Si of SiO₂ (Fig. 3e₃) [27]. It was worth noting that the binding energy of O1s was 533.1 eV (Fig. 3e₄), which was higher than that of Fe₃O₄ (529.6 eV) by 3.5 eV. This was mainly due to the formation of Fe-O-Si chemical bond (530.2 eV) decreased the electronic density of O binding Fe, resulting in the chemical shift of binding energy of O1s. Moreover, the coexistence of Si-O-Si and Fe-O-Si verified the coating of SiO₂ on the nanochains.

The XRD patterns of Fe₃O₄ nanoparticles and Fe₃O₄@SiO₂ nanochains were exhibited in Fig. 3f. There were typical diffraction peaks of (200), (311), (400), (422), (511) and (440) planes, which corresponded to Fe₃O₄ presented in both patterns, confirming that the crystal structure of Fe₃O₄ nanoparticles were completely preserved during the synthesis of Fe₃O₄@SiO₂. Compared with Fe₃O₄, a new broad diffraction at around 20° appeared in Fe₃O₄@SiO₂, which was attributed to the amorphous SiO₂ shell [28]. In the FTIR spectrum (Fig. 3g), the absorption peak at 1076 cm⁻¹ in Fe₃O₄@SiO₂ was ascribed to Si-O bond while the peak at 592 cm⁻¹ was attributed to Fe-O bond [29–31], which further confirmed that the core-shell structure of Fe₃O₄@SiO₂ nanochains.

Physical and chemical properties

The porous scaffold with honeycomb structure was shown in Fig. 4a. The pore size of the scaffold was 800 ± 50 μm, which was proven to be beneficial to cell adhesion and climbing growth [32]. The magnetic behaviors of the PLLA, PLLA/Fe₃O₄ and PLLA/Fe₃O₄@SiO₂ scaffolds were shown in Figs. 4b and 4c. It was clearly seen that the introduction of Fe₃O₄ and Fe₃O₄@SiO₂ endowed the non-magnetic PLLA scaffold favorable magnetic properties (Figs. 4b). Although the magnetic saturation intensity of the PLLA/Fe₃O₄@SiO₂ scaffold was slightly lower than that of the PLLA/Fe₃O₄ scaffold, the low remanence (*M_r*) similar to Fe₃O₄ proved that the PLLA/Fe₃O₄@SiO₂ scaffold still possessed good superparamagnetism (Fig. 4c). This was conducive to construct magnetic microenvironment in scaffold, which was expected to enhance cell viability and promote cell growth through magnetic stimulation.

The phase composition of the scaffolds was assessed using XRD (Fig. 4d). It can be clearly observed that the diffraction peaks belonged to (010), (110), (203) and (205) planes of PLLA [33]. By contrast, the new diffraction peaks corresponding to (311), (400), (551) and (440) crystal planes confirmed the spinel structure of Fe₃O₄ in PLLA/Fe₃O₄ and PLLA/Fe₃O₄@SiO₂ scaffolds [34].

Generally, a scaffold with favorable hydrophilicity is more conducive to cell adhesion [35]. The hydrophilicity of PLLA, PLLA/Fe₃O₄ and PLLA/Fe₃O₄@SiO₂ scaffolds was investigated via water contact

angle test. As shown in Fig. 4e, the contact angle on the PLLA scaffold was $86.2 \pm 2.8^\circ$. By contrast, the contact angle decreased after the adding Fe_3O_4 nanoparticles, indicating the improvement of hydrophilicity. This could be attributed to the presence of hydroxyl groups on the Fe_3O_4 nanoparticles in aqueous environment. Moreover, the PLLA/ Fe_3O_4 @ SiO_2 scaffolds exhibited the best hydrophilicity, which was mainly due to the silanol groups of SiO_2 absorbed water molecule via hydrogen bonding.

Cytocompatibility

The cytocompatibility of scaffolds is a necessary and crucial element in the bone repair process because it determines whether cells can adhere, grow, and proliferate on the scaffold [36]. Herein, the cytocompatibility of the PLLA, PLLA/ Fe_3O_4 and PLLA/ Fe_3O_4 @ SiO_2 scaffolds were assessed. As shown in Fig. 5a, cells adhered well on all scaffolds, indicating that the PLLA, PLLA/ Fe_3O_4 and PLLA/ Fe_3O_4 @ SiO_2 scaffolds had good biocompatibility. Particularly, better cell adhesion morphology displayed on PLLA/ Fe_3O_4 @ SiO_2 scaffold than that on PLLA and PLLA/ Fe_3O_4 scaffolds at the same time point. Moreover, the cells completely expanded and essentially presented normal topological configuration on PLLA/ Fe_3O_4 @ SiO_2 scaffold after 7 days of cultivation, indicating that the Fe_3O_4 @ SiO_2 nanochains in scaffold were more conducive to cell adhesion and expansion.

Cell viability is also an important indicator for evaluating the cytocompatibility of the scaffold [37–39]. To investigate the cells viability induced by the PLLA, PLLA/ Fe_3O_4 and PLLA/ Fe_3O_4 @ SiO_2 scaffolds, the cells were strained with calcein AM. Normally, calcein AM only stains living cells, because calcein AM as a dye can be transformed into a membrane impermeable fluorescent analogue by the cell esterases, and the fluorescence will leak out when the cell membrane is completely damaged [40, 41]. As shown in Fig. 5b, the density of living cells in PLLA, PLLA/ Fe_3O_4 and PLLA/ Fe_3O_4 @ SiO_2 scaffold groups was significantly enhanced with time, confirming that all scaffolds possessed the ability to enhance cell activity. Notably, the cells increased exponentially from 3 to 7 days with the highest density observing in the cells which cocultured with PLLA/ Fe_3O_4 @ SiO_2 scaffold, indicating that the Fe_3O_4 @ SiO_2 nanochains in scaffold significantly enhanced cell viability and promoted cell proliferation.

Cell proliferation is one of the important physiological functions of living cells[42]. To quantitatively study the cell proliferation capacity on the PLLA, PLLA/ Fe_3O_4 and PLLA/ Fe_3O_4 @ SiO_2 scaffolds, the CCK-8 assay was carried out (Fig. 5c). It could be clearly seen that the optical density (OD) value of cells on all the scaffolds increased significantly with incubating time. Compared with the PLLA scaffold, higher OD value of cells presented on the PLLA/ Fe_3O_4 scaffold, indicating that the Fe_3O_4 nanoparticles in the scaffold promoted cell proliferation. Especially, the OD value of cells on PLLA/ Fe_3O_4 @ SiO_2 scaffold was markedly higher than that on PLLA/ Fe_3O_4 scaffold, indicating that the Fe_3O_4 @ SiO_2 nanochains further promoted cell proliferation.

As one of the early indicators of osteogenic differentiation [43], ALP activity of cells cultured on the scaffolds for 7 days was qualitatively analyzed (Fig. 6a). It could be clearly seen that the cells cocultured with the PLLA/ Fe_3O_4 @ SiO_2 scaffold samples exhibited higher ALP activity than PLLA and PLLA/ Fe_3O_4

samples. As one of the late markers of osteogenic differentiation [44], the Alizarin Red staining was performed to assess the extracellular matrix mineralization of cells cocultured with the scaffolds for 7 days (Fig. 6b). As expected, there were obvious red precipitates in all scaffold groups. It was worth noting that the mineral deposition was significantly enhanced in PLLA/Fe₃O₄@SiO₂ samples compared to other groups, mainly due to the stronger magnetic stimulation effect of Fe₃O₄@SiO₂ nanochains. The above results demonstrated that the Fe₃O₄@SiO₂ nanochains in scaffold markedly enhanced cell activity and promoted cell proliferation, differentiation, and mineralization.

The bone-related gene expressions including RUNX2, OPN, OCN and OSX on PLLA, PLLA/Fe₃O₄ and PLLA/Fe₃O₄@SiO₂ scaffolds were investigated (Fig. 7). From an overall perspective, the expression levels of RUNX2, OPN, OCN and OSX on day 7 were greatly higher than on day 3. Especially, the expression level of them on the PLLA/Fe₃O₄@SiO₂ scaffold were markedly higher than that on PLLA/Fe₃O₄ and PLLA scaffolds at any time. The results showed that the Fe₃O₄@SiO₂ nanochains provided a more favorable magnetic microenvironment for cell differentiation than Fe₃O₄ nanoparticles in scaffolds, confirming that the superior capability of Fe₃O₄@SiO₂ nanochains to promote cell differentiation.

Discussion

It is well known that various cells, such as mesenchymal stem cells, osteoblasts, and endothelial cells are magnetically sensitive due to the diamagnetism of cell membranes [45]. Inspired by these, researchers have applied different external magnetic fields to study the roles of magnetic stimulation in bone repair in recent years [46, 47]. It was found that the external magnetic fields could induce a series of cell behaviors by regulating cell surface receptors and signaling pathways via magnetic stimulations, thereby accelerating new bone regeneration or inhibiting osteoclast resorption. However, the need of magnetic field generators limits the clinical application of magnetic stimulation to a certain extent.

To solve the above problem, it would be an effective means to construct an endogenous magnetic microenvironment in bone scaffolds by introducing magnetic materials. As a highly biocompatible and magnetic materials, Fe₃O₄ nanoparticles have received clinical approval from the Food and Drug Administration. The scaffolds loaded with Fe₃O₄ nanoparticles indeed effectively enhanced cell viability and promoted cell proliferation [48, 49]. However, the random arrangement of Fe₃O₄ nanoparticles in the scaffolds greatly compromised their positive magnetic stimulation effects, due to the mutual repulsive between adjacent magnetic dipoles.

In present study, we constructed Fe₃O₄@SiO₂ nanochains with uniform shell-core structure by magnetic-field-guided interface co-assembly of Fe₃O₄ nanoparticles (Fig. 2). The simulation analysis results of magnetic field distribution proved the orderly assembly of Fe₃O₄ nanoparticles in the Fe₃O₄@SiO₂ nanochains formed magnetic energy coupling and obtained a highly magnetic micro-field (Figs. 3a-c). The results are consistent with the analysis of Yin Yadong's team [50–52]. From the results of magnetic tests, the Fe₃O₄@SiO₂ nanochains still preserved the superior superparamagnetism of Fe₃O₄

nanoparticles. The good magnetism and high surface areas endowed $\text{Fe}_3\text{O}_4@\text{SiO}_2$ nanochains with great potential for use in biomedicine.

To better understand the biological advantages of $\text{Fe}_3\text{O}_4@\text{SiO}_2$ nanochains in scaffolds, a series of *in vitro* cell experiments were performed. Compared to PLLA/ Fe_3O_4 scaffolds, PLLA/ $\text{Fe}_3\text{O}_4@\text{SiO}_2$ scaffolds are more conducive to cell adhesion and expansion, especially further enhancing cell viability, proliferation, differentiation, mineralization, and bone-related gene expressions (Figs. 5–7). It could be attributed to the stronger magnetic stimulation effect of $\text{Fe}_3\text{O}_4@\text{SiO}_2$ nanochains. In terms of mechanism, the orderly assembly of Fe_3O_4 nanoparticles obtained magnetic energy coupling, resulting in a highly micro-field that stimulated the surrounding cells to respond (Fig. 8). In this case, the membrane flux of the diamagnetic cell membrane would be modified. Moreover, the strong magnetic singles would activate receptors on the cell membrane, thereby modulating a series of signaling pathways including Ca^{2+} channels, mitogen-activated protein kinase (MAPK), bone morphogenetic protein-2 (BMP-2) and integrins [5, 9, 43, 53]. Then, the corresponding downstream transcription factors were regulated, and consequently osteogenesis-related gene expressions of RUNX2, OPN, OCN and OSX were up-regulated. Hence, the $\text{Fe}_3\text{O}_4@\text{SiO}_2$ nanochains in scaffold possessed great potential in accelerating bone repair.

Conclusions

A magnetic-field-guided interface co-assembly of Fe_3O_4 nanoparticles had been demonstrated to rationally synthesis unique $\text{Fe}_3\text{O}_4@\text{SiO}_2$ nanochains. The obtained $\text{Fe}_3\text{O}_4@\text{SiO}_2$ nanochains exhibited high magnetic susceptibility and excellent magnetic induction intensity. Importantly, the superior magnetic properties of nanochains enhanced the interaction between PLLA/ $\text{Fe}_3\text{O}_4@\text{SiO}_2$ scaffold and cells. As a result, the nanochains in scaffold effectively enhanced cell activity, proliferation, differentiation, and mineralization as well as bone-related gene expressions. These findings confirmed the superparamagnetic scaffold incorporated with $\text{Fe}_3\text{O}_4@\text{SiO}_2$ nanochains could accelerate the repair of bone defect.

Abbreviations

PLLA

Poly L-lactic acid

SiO_2

Silica

SLS

Selective laser sintering

TEOS

Tetraethoxysilicate

TEM

Transmission electron microscope

XPS
X-ray photoelectron spectrometer
FTIR
Fourier transform infra-red spectrometer
XRD
X-ray diffractometer
VSM
Vibrating sample magnetometer
DMEM
Dulbecco's Modified Eagle's Medium
SEM
Scanning electron microscope
CCK-8
Cell Counting Kit-8
ALP
Alkaline phosphatase
Runx2
Runt-related transcription factor-2
OPN
Osteopontin
OCN
Osteocalcin
OSX
Osterix.

Declarations

Ethics approval and consent to participate

Not applicable.

Consent for publication

Not applicable.

Availability of data and materials

The datasets used and/or analysed during the current study are available from the corresponding author on reasonable request.

Competing interests

The authors declare that they have no competing interests.

Funding

This study was supported by the following funds: (1) The Natural Science Foundation of China (52105352, 51935014, 52165043, 82072084, 81871498); (2) The Project of Jiangxi University of Science and Technology (205200100535); (3) JiangXi Provincial Natural Science Foundation of China (2020ACB214004, 20202BAB214011); (4) The Provincial Key R&D Projects of Jiangxi (20201BBE51012); (5) The Project of State Key Laboratory of High Performance Complex Manufacturing.

Authors' contributions

Shuai CJ and Chen X contributed to acquisition, analysis of data, drafted and revised the manuscript. He CX, Qian GW and Shuai Y contributed to analysis and interpretation of the data. Yao J, Xu WD and Peng SP contributed to performing the experiments. Deng YW and Yang WJ conceptualized the experimental research, acquired the financial support/experimental resources, supervised the research activities, validated the data and reviewed the paper. All authors read and approved the final manuscript.

Acknowledgments

Not applicable.

References

- [1] M. Zhang, R. Lin, X. Wang, J. Xue, C. Deng, C. Feng, H. Zhuang, J. Ma, C. Qin, L. Wan, 3D printing of Haversian bone-mimicking scaffolds for multicellular delivery in bone regeneration, *Science advances* 6(12) (2020) eaaz6725.
- [2] Z. Othman, H. Fernandes, A.J. Groot, T.M. Luider, A. Alcinesio, D. de Melo Pereira, A.P. Guttenplan, H. Yuan, P. Habibovic, The role of ENPP1/PC-1 in osteoinduction by calcium phosphate ceramics, *Biomaterials* 210 (2019) 12-24.
- [3] S. Pina, J.M. Oliveira, R.L. Reis, Natural-based nanocomposites for bone tissue engineering and regenerative medicine: a review, *Advanced Materials* 27(7) (2015) 1143-1169.
- [4] W.Z. Lew, S.W. Feng, S.Y. Lee, H.M. Huang, The review of bioeffects of static magnetic fields on the oral tissue-derived cells and its application in regenerative medicine, *Cells* 10(10) (2021) 2662.

- [5] Y. Xia, J. Sun, L. Zhao, F. Zhang, X.J. Liang, Y. Guo, M.D. Weir, M.A. Reynolds, N. Gu, H.H. Xu, Magnetic field and nano-scaffolds with stem cells to enhance bone regeneration, *Biomaterials* 183 (2018) 151-170.
- [6] Y. Kong, J. Duan, F. Liu, L. Han, G. Li, C. Sun, Y. Sang, S. Wang, F. Yi, H. Liu, Regulation of stem cell fate using nanostructure-mediated physical signals, *Chemical Society Reviews* (2021).
- [7] Y. Qiao, X. Liu, B. Li, Y. Han, Y. Zheng, K.W.K. Yeung, C. Li, Z. Cui, Y. Liang, Z. Li, Treatment of MRSA-infected osteomyelitis using bacterial capturing, magnetically targeted composites with microwave-assisted bacterial killing, *Nature communications* 11(1) (2020) 1-13.
- [8] S. Khizar, N.M. Ahmad, N. Zine, N. Jaffrezic-Renault, A. Errachid-el-salhi, A. Elaissari, Magnetic nanoparticles: From synthesis to Theranostic applications, *ACS Applied Nano Materials* 4(5) (2021) 4284-4306.
- [9] H.M. Yun, S.J. Ahn, K.R. Park, M.J. Kim, J.J. Kim, G.Z. Jin, H.W. Kim, E.C. Kim, Magnetic nanocomposite scaffolds combined with static magnetic field in the stimulation of osteoblastic differentiation and bone formation, *Biomaterials* 85 (2016) 88-98.
- [10] J. Li, X. Lu, Y. Zhang, F. Cheng, Y. Li, X. Wen, S. Yang, Transmittance tunable smart window based on magnetically responsive 1D nanochains, *ACS Applied Materials & Interfaces* 12(28) (2020) 31637-31644.
- [11] Q. Xiong, C.Y. Lim, J. Ren, J. Zhou, K. Pu, M.B. Chan-Park, H. Mao, Y.C. Lam, H. Duan, Magnetic nanochain integrated microfluidic biochips, *Nature communications* 9(1) (2018) 1-11.
- [12] M. Ma, Q. Zhang, J. Dou, H. Zhang, D. Yin, W. Geng, Y. Zhou, Fabrication of one-dimensional $\text{Fe}_3\text{O}_4/\text{P}(\text{GMA-DVB})$ nanochains by magnetic-field-induced precipitation polymerization, *Journal of colloid and interface science* 374(1) (2012) 339-344.
- [13] M. Ma, Q. Zhang, H. Zhang, T. Xin, B. Zhang, X. Fan, One-Pot Synthesis of Highly Magnetically Sensitive Nanochains Coated with a Fluorescent Shell by Magnetic-Field-Induced Precipitation Polymerization, *Science of Advanced Materials* 5(6) (2013) 623-629.
- [14] J. Sun, X. Liu, J. Huang, L. Song, Z. Chen, H. Liu, Y. Li, Y. Zhang, N. Gu, Magnetic assembly-mediated enhancement of differentiation of mouse bone marrow cells cultured on magnetic colloidal assemblies, *Scientific reports* 4(1) (2014) 1-8.
- [15] J. Zhou, C. Wang, P. Wang, P.B. Messersmith, H. Duan, Multifunctional magnetic nanochains: exploiting self-polymerization and versatile reactivity of mussel-inspired polydopamine, *Chemistry of Materials* 27(8) (2015) 3071-3076.
- [16] J. Jia, J.C. Yu, Y.X.J. Wang, K.M. Chan, Magnetic nanochains of FeNi_3 prepared by a template-free microwave-hydrothermal method, *ACS applied materials & interfaces* 2(9) (2010) 2579-2584.

- [17] X. Li, L. Sun, H. Wang, K. Xie, Q. Long, X. Lai, L. Liao, Synthesis of cobalt nanowires in aqueous solution under an external magnetic field, *Beilstein Journal of Nanotechnology* 7(1) (2016) 990-994.
- [18] J. Zhang, W. Xiang, Y. Liu, M. Hu, K. Zhao, Synthesis of high-aspect-ratio nickel nanowires by dropping method, *Nanoscale Research Letters* 11(1) (2016) 1-5.
- [19] A. Saha, H. Ben Halima, A. Saini, J. Gallardo-Gonzalez, N. Zine, C. Viñas, A. Elaissari, A. Errachid, F. Teixidor, Magnetic Nanoparticles Fishing for Biomarkers in Artificial Saliva, *Molecules* 25(17) (2020) 3968.
- [20] M. Tarhini, J. Vega-Chacón, M. Jafelicci, N. Zine, A. Errachid, H. Fessi, A. Elaissari, Structured magnetic core/silica internal shell layer and protein out layer shell (BSA@SiO₂@SME): preparation and characterization, *Chemistry Africa* 3(1) (2020) 127-134.
- [21] A. Bitar, J. Vega-Chacón, Z. Lgourna, H. Fessi, M. Jafelicci Jr, A. Elaissari, Submicron silica shell-magnetic core preparation and characterization, *Colloids and Surfaces A: Physicochemical and Engineering Aspects* 537 (2018) 318-324.
- [22] F. Qi, R. Liao, Y. Shuai, H. Pan, G. Qian, S. Peng, C. Shuai, A conductive network enhances nerve cell response, *Additive Manufacturing* (2022) 102694.
- [23] L. Yu, T. He, J. Yao, W. Xu, S. Peng, P. Feng, C. Shuai, Cu ions and cetyltrimethylammonium bromide loaded into montmorillonite: a synergistic antibacterial system for bone scaffolds, *Materials Chemistry Frontiers* 6(1) (2022) 103-116.
- [24] S. Kralj, D. Makovec, Magnetic assembly of superparamagnetic iron oxide nanoparticle clusters into nanochains and nanobundles, *ACS nano* 9(10) (2015) 9700-9707.
- [25] S. Kralj, T. Potrc, P. Kocbek, S. Marchesan, D. Makovec, Design and fabrication of magnetically responsive nanocarriers for drug delivery, *Current medicinal chemistry* 24(5) (2017) 454-469.
- [26] A. Nikmah, A. Taufiq, A. Hidayat, Sunaryono, H. Susanto, Excellent Antimicrobial Activity of Fe₃O₄/SiO₂/Ag Nanocomposites, *Nano* 16(05) (2021) 2150049.
- [27] A. Rajan, M. Sharma, N.K. Sahu, Assessing magnetic and inductive thermal properties of various surfactants functionalised Fe₃O₄ nanoparticles for hyperthermia, *Scientific reports* 10(1) (2020) 1-15.
- [28] L. Wang, C. Shen, Y. Cao, PVP modified Fe₃O₄@SiO₂ nanoparticles as a new adsorbent for hydrophobic substances, *Journal of Physics and Chemistry of Solids* 133 (2019) 28-34.
- [29] Z. Chen, H. Wang, Y. Wang, R. Lv, X. Yang, J. Wang, L. Li, W. Ren, Improved optical damage threshold graphene Oxide/SiO₂ absorber fabricated by sol-gel technique for mode-locked erbium-doped fiber lasers, *Carbon* 144 (2019) 737-744.

- [30] J. Chen, M. Qiao, W. Wang, Q. Zhang, A novel magnetic mesoporous $\text{Fe}_3\text{O}_4@\text{Void}@m\text{SiO}_2\text{-Pd}(0)$ nanochains with high heterogeneous catalysis efficiency for Suzuki coupling reaction, *Composites Communications* 16 (2019) 41-49.
- [31] P. Feng, J. Jia, S. Peng, Y. Shuai, H. Pan, X. Bai, C. Shuai, Transcrystalline growth of PLLA on carbon fiber grafted with nano- SiO_2 towards boosting interfacial bonding in bone scaffold, *Biomaterials Research* 26(1) (2022) 1-15.
- [32] M. Maniruzzaman, 3D and 4D printing in biomedical applications: process engineering and additive manufacturing, John Wiley & Sons 2019.
- [33] F. Beltrán, M. De La Orden, V. Lorenzo, E. Pérez, M. Cerrada, J.M. Urreaga, Water-induced structural changes in poly (lactic acid) and PLLA-clay nanocomposites, *Polymer* 107 (2016) 211-222.
- [34] L. Yang, P. Zou, J. Cao, Y. Sun, D. Han, S. Yang, G. Chen, X. Kong, J. Yang, Facile synthesis and paramagnetic properties of $\text{Fe}_3\text{O}_4@\text{SiO}_2$ core-shell nanoparticles, *Superlattices and Microstructures* 76 (2014) 205-212.
- [35] R. Augustine, P. Dan, I. Schlachet, D. Rouxel, P. Menu, A. Sosnik, Chitosan ascorbate hydrogel improves water uptake capacity and cell adhesion of electrospun poly (epsilon-caprolactone) membranes, *International Journal of Pharmaceutics* 559 (2019) 420-426.
- [36] H. Liang, Y. Yang, D. Xie, L. Li, N. Mao, C. Wang, Z. Tian, Q. Jiang, L. Shen, Trabecular-like Ti-6Al-4V scaffolds for orthopedic: fabrication by selective laser melting and in vitro biocompatibility, *Journal of Materials Science & Technology* 35(7) (2019) 1284-1297.
- [37] C. Shuai, L. Yu, P. Feng, S. Peng, H. Pan, X. Bai, Construction of a stereocomplex between poly (d-lactide) grafted hydroxyapatite and poly (l-lactide): toward a bioactive composite scaffold with enhanced interfacial bonding, *Journal of Materials Chemistry B* (2022).
- [38] D.M. González-García, Á. Marcos-Fernández, L.M. Rodríguez-Lorenzo, R. Jiménez-Gallegos, N. Vargas-Becerril, L. Téllez-Jurado, Synthesis and in vitro cytocompatibility of segmented poly (ester-urethane) s and poly (ester-urea-urethane) s for bone tissue engineering, *Polymers* 10(9) (2018) 991.
- [39] C. Gao, M. Yao, S. Peng, W. Tan, C. Shuai, Pre-oxidation induced in situ interface strengthening in biodegradable Zn/nano-SiC composites prepared by selective laser melting, *Journal of Advanced Research* (2021).
- [40] S. Bhattacharyya, S.S. Ghosh, Transmembrane TNF α -expressed macrophage membrane-coated chitosan nanoparticles as cancer therapeutics, *ACS omega* 5(3) (2020) 1572-1580.
- [41] Y. Zhang, S. Liu, Y. Yao, Y. Chen, S. Zhou, X. Yang, K. Wang, J. Liu, Invasion and Defense Interactions between Enzyme-Active Liquid Coacervate Protocells and Living Cells, *Small* 16(29) (2020) 2002073.

- [42] Y. Yang, Y. Cheng, M. Yang, G. Qian, S. Peng, F. Qi, C. Shuai, Semicoherent strengthens graphene/zinc scaffolds, *Materials Today Nano* 17 (2022) 100163.
- [43] H. Chen, J. Sun, Z. Wang, Y. Zhou, Z. Lou, B. Chen, P. Wang, Z. Guo, H. Tang, J. Ma, Magnetic cell-scaffold interface constructed by superparamagnetic IONP enhanced osteogenesis of adipose-derived stem cells, *ACS applied materials & interfaces* 10(51) (2018) 44279-44289.
- [44] H. Wang, X. Zeng, L. Pang, H. Wang, B. Lin, Z. Deng, E.L.X. Qi, N. Miao, D. Wang, P. Huang, Integrative treatment of anti-tumor/bone repair by combination of MoS₂ nanosheets with 3D printed bioactive borosilicate glass scaffolds, *Chemical Engineering Journal* 396 (2020) 125081.
- [45] J. Yang, H. Zhang, P. Shang, Effect of static magnetic field on bone and its molecular mechanism, *Chinese Science Bulletin* 65(13) (2020) 1238-1250.
- [46] H.Y. Xu, N. Gu, Magnetic responsive scaffolds and magnetic fields in bone repair and regeneration, *Frontiers of Materials Science* 8(1) (2014) 20-31.
- [47] J. Zan, G. Qian, F. Deng, J. Zhang, Z. Zeng, S. Peng, C. Shuai, Dilemma and breakthrough of biodegradable poly-l-lactic acid in bone tissue repair, *Journal of Materials Research and Technology* (2022).
- [48] U. Anjaneyulu, B. Priyadarshini, U. Vijayalakshmi, Preparation of Ag doped hydroxyapatite-Fe₃O₄-chitosan composites: In vitro biocompatibility study on MG-63 cells for orthopedic applications, *Advanced Science Letters* 24(8) (2018) 5901-5906.
- [49] Z.C. Wu, W.P. Li, C.H. Luo, C.H. Su, C.S. Yeh, Rattle-Type Fe₃O₄@ CuS Developed to Conduct Magnetically Guided Photoinduced Hyperthermia at First and Second NIR Biological Windows, *Advanced Functional Materials* 25(41) (2015) 6527-6537.
- [50] Z. Li, F. Yang, Y. Yin, Smart materials by nanoscale magnetic assembly, *Advanced Functional Materials* 30(2) (2020) 1903467.
- [51] Z. Li, M. Wang, X. Zhang, D. Wang, W. Xu, Y. Yin, Magnetic assembly of nanocubes for orientation-dependent photonic responses, *Nano Letters* 19(9) (2019) 6673-6680.
- [52] M. Wang, L. He, Y. Yin, Magnetic field guided colloidal assembly, *Materials Today* 16(4) (2013) 110-116.
- [53] Y. Zhu, Q. Yang, M. Yang, X. Zhan, F. Lan, J. He, Z. Gu, Y. Wu, Protein corona of magnetic hydroxyapatite scaffold improves cell proliferation via activation of mitogen-activated protein kinase signaling pathway, *ACS nano* 11(4) (2017) 3690-3704.

Figures

(a) Magnetic field distribution around a Fe_3O_4 nanoparticle. The attractive (b) dipole-dipole forces between two adjacent nanoparticles drive the formation of nanochains along the magnetic field (c). (d) Magnetization curves, (e) XPS spectra of $\text{Fe}_3\text{O}_4@ \text{SiO}_2$ nanochains. (e₁) XPS survey spectrum along with the spectra of (e₂) Fe2p, (e₃) Si2p and (e₄) O1s. (f) XRD patterns, (g) FTIR spectra.

Figure 4

(a) Optical graphs of SLS prepared honeycomb scaffold. (b) Magnetization curves. (c) magnetization behaviors at magnetic field from -90 to 90 Oe. (d) XRD patterns and (e) hydrophilicity of PLLA, PLLA/ Fe_3O_4 and PLLA/ $\text{Fe}_3\text{O}_4@ \text{SiO}_2$ scaffolds.

Figure 5

(a) Adhesion morphologies of MG-63 cells on PLLA, PLLA/ Fe_3O_4 and PLLA/ $\text{Fe}_3\text{O}_4@ \text{SiO}_2$ scaffolds. (b) Fluorescence images of cells cultured after 3 and 7 days on the scaffolds. (c) Cell proliferation on the scaffolds.



Figure 6

(a) The ALP and (b) Alizarin Red staining of cells on PLLA, PLLA/ Fe_3O_4 and PLLA/ $\text{Fe}_3\text{O}_4@ \text{SiO}_2$ scaffolds after 7 days of cultivation.

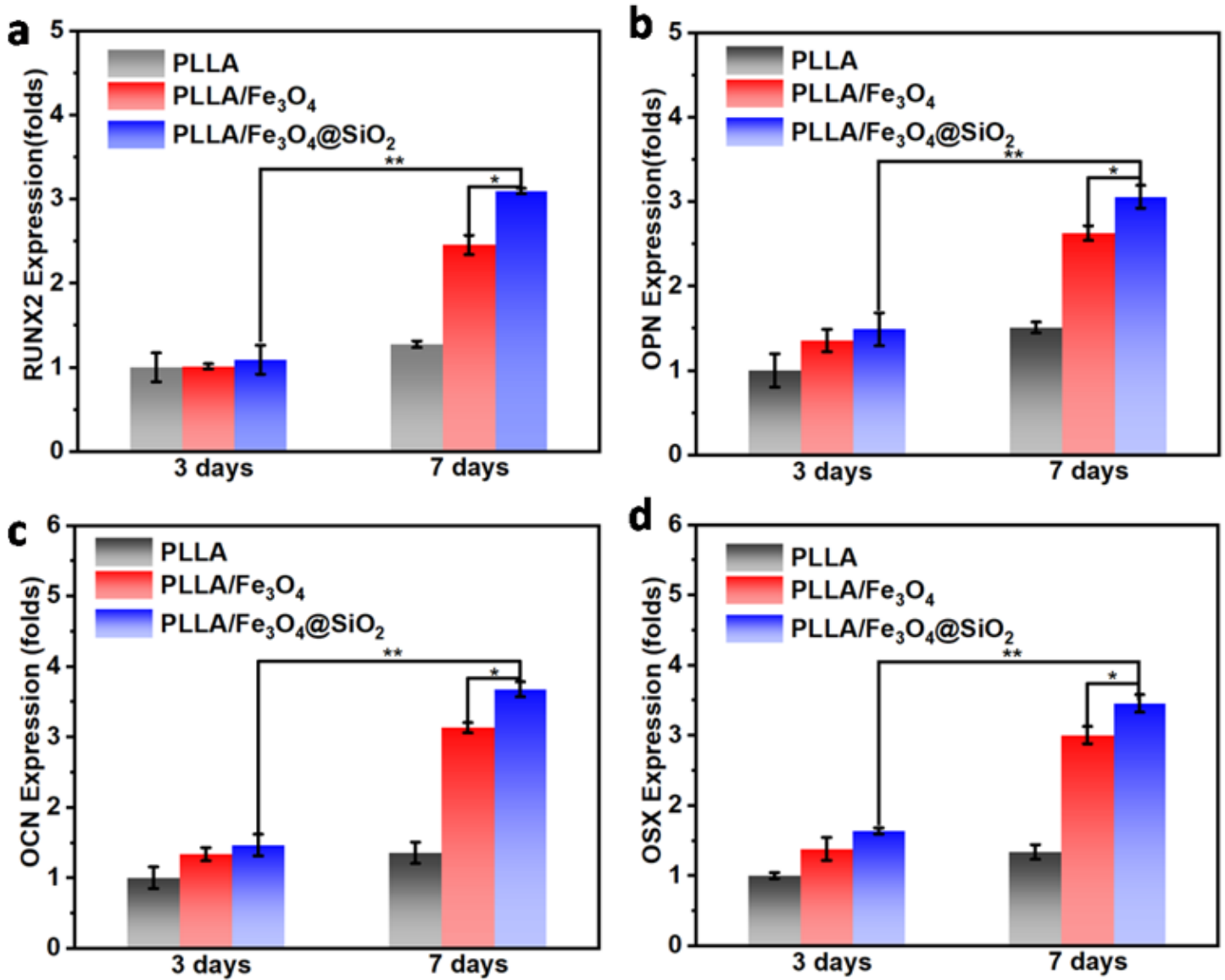


Figure 7

The expressions of (a) RUNX2, (b) OPN, (c) OCN and (d) OSX on the scaffolds after 3 and 7 days of culture.



Figure 8

Schematic illustration of $\text{Fe}_3\text{O}_4@\text{SiO}_2$ magnetic nanochains in up-regulating osteogenesis-related gene expressions.